Turkish Journal of Electrical Engineering & Computer Sciences

http://journals.tubitak.gov.tr/elektrik/

Research Article

Turk J Elec Eng & Comp Sci
(2017) 25: 2491 – 2500
© TÜBİTAK
doi:10.3906/elk-1604-203

Thermomechanical MEMS membranes for fiber optic temperature sensing

Onur FERHANOĞLU*
Department of Electrical and Communication Engineering, İstanbul Technical University, İstanbul, Turkey

Received: 15.04.2016 • **Accepted/Published Online:** 20.09.2016 • **Final Version:** 29.05.2017

Abstract: In this study, the design, fabrication, and characterization results of square and circular cross-sectioned, bimaterial microelectromechanical system (MEMS) membranes are presented. The MEMS structures, having width of 250 μm to 1.5 mm and 1–4 mm^2 die area, were designed towards integration on a single-mode fiber tip for temperature-sensing. Embedded diffraction grating underneath each membrane allows for interferometric detection of thermomechanical response through backside laser illumination. The displacement of MEMS membranes was monitored under direct heating, revealing 50–1800 nm/$^\circ$C thermomechanical sensitivity range. Furthermore, atomic force microscopy-based stiffness measurement on the MEMS membranes revealed a spring constant within 2–30 N/m range. Temperature measurement range and speed of the MEMS sensors were thoroughly tabulated based on experimental findings, as well as finite-element simulations and analytical calculations. Finally, proof-of-concept testing of a selected device was accomplished through air-coupling of the MEMS structure with a gradient index-collimated fiber, revealing $<$35 m$^\circ$C temperature sensitivity using a low-cost laser source and detector.

Key words: Microelectromechanical systems, temperature measurement, microfabrication

1. Introduction

Integration of microelectromechanical systems (MEMS) with optical fibers has allowed for high-sensitivity detection at low cost for various applications, including pressure [1,2] and temperature sensing [3]. The wide use of thermomechanical MEMS structures in thermal imaging applications [4,5] has also leveraged their utilization in fiber optic temperature sensors, as the moving arm of the in-line interferometer. Recently, we proposed and demonstrated a fiber temperature sensor, utilizing a 1-mm width and square-framed bimaterial MEMS membrane that was coupled to a gradient index (GRIN)-collimated single-mode fiber [3]. In this study, we present the design, fabrication, and characterization results for a plethora of circular and square-framed bimaterial membranes of different sizes. We further deduce the temperature measurement range of the sensors, based on the measured thermomechanical sensitivity, and the sensor gap that sets a limit on the membrane motion.

Figure 1a presents the floor plan and microscope image of the chip, which has 1 $\times$ 1 cm^2 area. The chip harbors 28 circular and square-framed sensors of 250 μm, 500 μm, 750 μm, 1000 μm, and 1500 μm in size (totaling 10 design variations), fabricated on 1 $\times$ 1 mm^2 and 2 $\times$ 2 mm^2 die areas. Figure 1b illustrates the proposed fiber optic sensor architecture, where a passive bimaterial MEMS membrane with underneath embedded diffraction is integrated into a GRIN collimated single mode fiber. Based on the die dimensions of

*Correspondence: ferhanoglu@itu.edu.tr

1×1 mm^2 and 2×2 mm^2 and the availability of <1 mm diameter GRIN lenses, the entire sensor can be encapsulated within 1–2 mm of diameter. Note that the interference signal diffracting of the membrane can be monitored through capturing the 0th order diffracted light that is recoupled back into the fiber, whereas higher orders are isolated owing to the gap between the GRIN lens and the sensor.

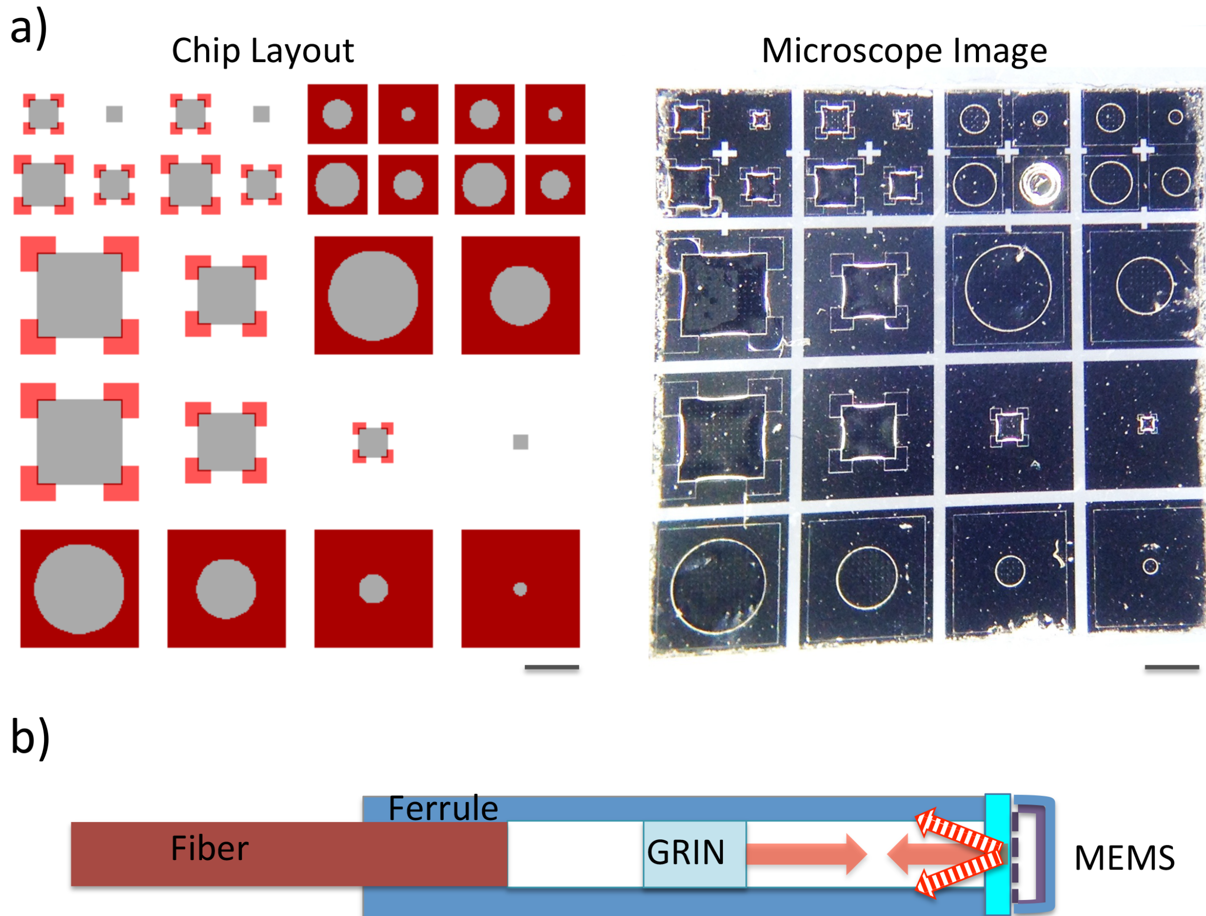

Figure 1. a) Chip layout and microscope image of the mother chip with 10 distinct sizes of square and circular-framed sensor membranes. Scale bar is 1 mm long; b) fiber optic sensor architecture utilizing bimaterial MEMS membranes.

2. Materials and methods

2.1. MEMS design and fabrication

MEMS membranes were designed as circular and square-framed table-shaped structures of 0.25–1.5 mm in size. Parylene was chosen as the structural layer of the membranes owing to its high coefficient of thermal expansion (CTE: 35 ppm/°C), allowing for high thermomechanical sensitivity. Along with parylene, titanium, which has a low CTE, serves both as the accompanying bimaterial layer and as the reflector of the in-line interferometer. The thickness of the layers was chosen as 2 μm for parylene and 200 nm for titanium, respectively, to mitigate cracking of the structural layer during fabrication while providing optimal thermomechanical sensitivity [6].

MEMS sensors were fabricated using a simple 4-mask process with standard processes, as described in detail in [3]. Briefly, the fabrication steps involve: 1) definition of the titanium layer on a transparent quartz substrate via lift-off as the grating layer; 2) definition of the anchors within the 5-μm-thick sacrificial photoresist,

followed by hard baking; 3) deposition and patterning of the 2-μm-thick parylene structural layer through a chemical vapor deposition process; and 4) sputtering and patterning of the top 200-nm-thick titanium layer to form the bimaterial structure, while providing the reflectivity for the moving arm of the in-line diffraction grating interferometer readout. Scanning electron microscope (SEM) images were acquired for circular and square-framed membranes following the fabrication process, as illustrated in Figure 2.

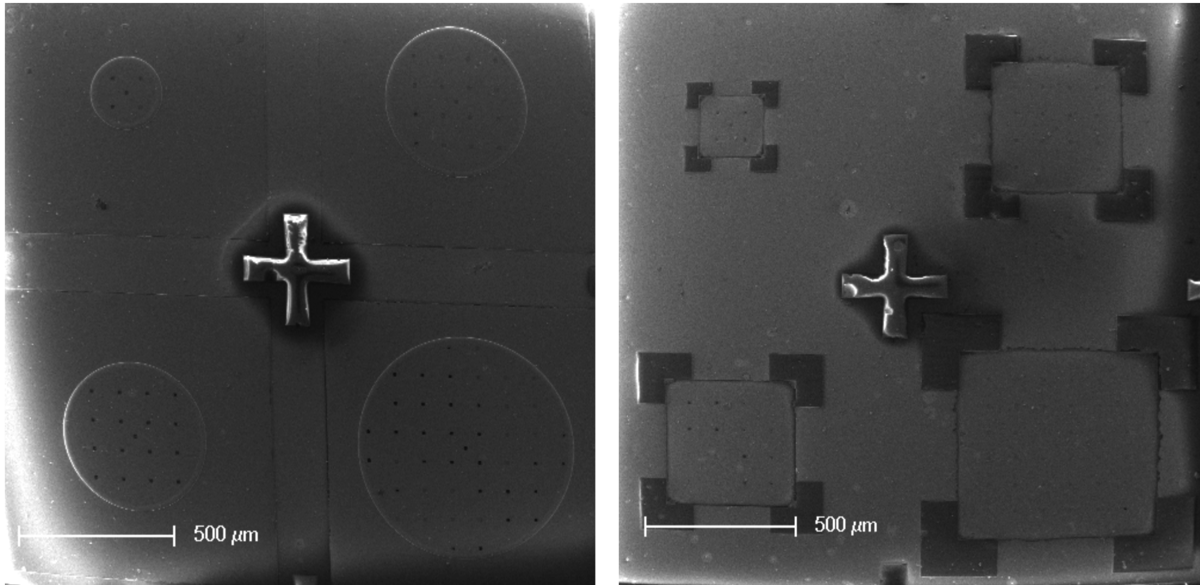

Figure 2. Scanning electron microscope images of 250 μm, 500 μm, and 750 μm MEMS membranes of circular and square shape.

The following paragraphs discuss the effects of sensor diameter, sacrificial layer height, and layer thicknesses on device performance parameters (thermomechanical sensitivity, speed, and measurement range). The displacement of a bimaterial structure (Δd) per applied temperature (ΔT) is dependent on the size of the device (where D is diameter for a circular-type membrane, width for a square-framed membrane, and length for a bimaterial cantilever), thickness (h_1, h_2), Young's moduli (E_1, E_2), and coefficient of thermal expansion (α_1, α_2) of both layers [6]:

$$\frac{\Delta d}{\Delta T} \sim \frac{E_1 E_2 h_1 h_2 (h_1 + h_2)(\alpha_1 - \alpha_2) D^2}{(E_1 h_1 + E_2 h_2)\left(E_1 h_1^3 + E_2 h_2^3\right) + 3 E_1 E_2 h_1 h_2 (h_1 + h_2)^2} \tag{1}$$

Note that the proportionality constant for the above equation varies depending on the type of bimaterial structure (cantilever, circular membrane, table-shaped device, etc.) The temperature range of the MEMS sensor ($<\mathrm{T}>$) is determined by the thermomechanical sensitivity ($\Delta d/\Delta T$) and the sacrificial layer thickness that sets the gap (g) between the device and the substrate, such that:

$$< \mathrm{T} > = \pm \frac{g}{\Delta d/\Delta T} \tag{2}$$

Improvement of the measurement range requires tailoring the thermomechanical sensitivity through a varying material type, layer thicknesses, and sensor sizes. Ultimately, increasing the sacrificial layer thickness will provide an improved measurement range without any sacrifice of thermomechanical sensitivity [3]. Sensor speed is yet

another crucial performance parameter that is determined by the heat capacity (C) and thermal conductivity (G) of the MEMS structure. Being analogous to a first-order electrical circuit consisting of a capacitor and a resistor, the thermal response time of the MEMS structure is calculated as [7]:

$$\tau = \frac{C}{\mathrm{G}} = \frac{\rho c V}{\mathrm{kA/L}} \tag{3}$$

where ρ is density, c is heat capacitance, and V is the volume of the sensor material. For a bimaterial sensor, the heat capacity is calculated as the sum of the heat capacities of both materials. On the other hand, thermal conductivity (G), which appears in the denominator of Eq. (3), is calculated as the product of thermal conductance (k), cross-sectional area (A), and reciprocal of the length (L) of the isolation region. For the fabricated sensors, the part that connects the membrane to the substrate constitutes the isolation region, where the sacrificial layer thickness (g) equals isolation length (L). For circular sensors, the membranes are connected to the substrate through a concentric cylinder that encircles the entire membrane (Figure 2). On the other hand, for table-framed sensors, the membrane is connected to the substrate via four legs, each of which has a width of one-fifth of that of the sensor. For simplification, the response time can be approximated by only considering the structural layers' heat capacity, which constitutes a great majority of the total heat capacity; the conductivity of the metal part, whose conductivity is dominant over both structural layers; and the conductivity of air.

2.2. Scaling rules for thermomechanical MEMS membranes

Table 1 presents the effects of the scaling of the sensor size (D), gap height (g), and layer thicknesses (h_1, h_2) on the device performance parameters, based on Eqs. (1)–(3). For simplicity, the ratio of layer thickness (parylene:titanium – 10:1) was kept constant to maintain optimal thermomechanical sensitivity. Assuming a scaling factor of a, varying the lateral sensor size from D to $a.D$ results in a thermomechanical sensitivity of $a^2.\Delta d/\Delta T$ (Eq. (1)) and a temperature measurement range of $<T>/a^2$ (Eq. (2)). Furthermore, considering the scaling of the volume and the cross-sectional area of the sensor, the response time is scaled as $a.\tau$ (Eq. (3)).

Table 1. Effect of scaling of the sensor size (D), gap height (g), and layer thickness (h_1, h_2) on the device performance parameters.

	Reference sensor	Scaling of sensor size	Scaling of sensor gap	Scaling of sensor thickness
Size, gap, thickness	D, g, h_i	$a.D$, g, h_i	D, $a.g$, h_i	D, g, $a.h_i$
Thermomechanical sensitivity	$\Delta d/\Delta T$	$a^2.\Delta d/\Delta T$	$\Delta d/\Delta T$	$\Delta d/\Delta T/a$
Measurement range	$<T>$	$<T>/a^2$	$a.<T>$	$a.<T>$
Sensor response time	τ	$a.\tau$	$a.\tau$	τ/a

The scaling of the sensor gap to $a.g$ has no effect on thermomechanical sensitivity, as the bimaterial membrane is solely responsible for the bending. On the other hand, the temperature measurement range and sensor response time scales to $a.<T>$ (Eq. (2)) and $a.\tau$(Eq. (3)), respectively, due to the change in gap thickness to $a.g$. Lastly, the change in layer thickness to $a.h_1$ and $a.h_2$, while preserving the thickness ratios, leads to a thermomechanical sensitivity of $\Delta d/\Delta T/a$(Eq. (1)). It also results in a temperature measurement range of $a.<T>$ (Eq. (2)) and a sensor response time of τ/a (Eq. (3)).

As a numerical example, doubling the sensor diameter quadruples the thermomechanical sensitivity while doubling the sensor thermal response time and dropping the temperature measurement range to a quarter of its initial value. On the other hand, doubling the sensor gap doubles both the temperature measurement range and the thermal time constant while preserving the thermomechanical sensitivity. Finally, doubling the layer thickness halves the thermomechanical sensitivity, doubles the temperature measurement range, and halves the thermal response time of the sensor.

2.3. Experimental setup

The testing of the fabricated chip, harboring a variety of MEMS thermomechanical membranes, was conducted using the setup illustrated in Figure 3. The chip, which was placed on a five-axis micromanipulator, was illuminated with a laser diode (1 mW in power, 635 nm in wavelength) that was coupled into a single mode fiber with a GRIN lens collimator at its distal end. The laser light that diffracted off the sensors was monitored using two photodetectors: the first one is placed at the distal end of the fiber that monitors the first-order diffracted light while the second is placed at the proximal end of the fiber, monitoring zero-order back-coupled light. The photodetector at the distal end is employed in thermal sensitivity measurements, and the photodetector at the proximal end is used in proof-of-concept temperature measurement experiments.

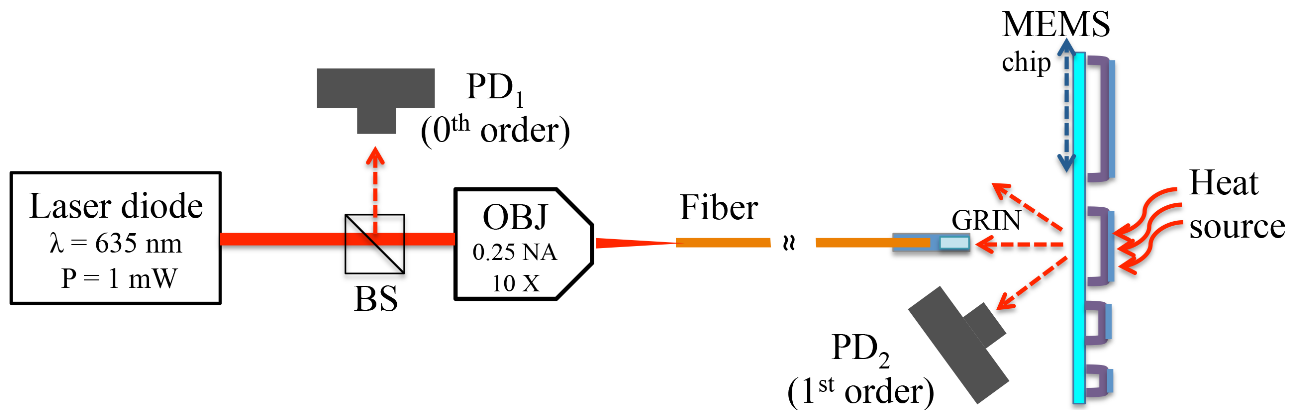

Figure 3. Experimental setup, illustrating illumination and collection optics, fiber coupling, and air-coupling of the MEMS chip, harboring multiple sensors back into the fiber.

3. Results

In the first set of experiments, a thermomechanical response of 10 distinct types of MEMS sensors, having a size of 250 μm to 1.5 mm, was performed using a heat source (soldering iron) that was placed at approximately 3 mm from the sensors. A digital thermometer (Maxim DS18B20) was also placed next to the chip as the reference temperature measurement. The distance between the heat source and the digital thermometer was adjusted to match the distance between the heat source and the MEMS chip. The thermomechanical sensitivity of the MEMS sensors to the heat source, illustrated in Figure 4, was calculated based on the fringe count of the observed first-order light intensity change at the distal end of the fiber and the absolute temperature increase that was observed by the digital thermometer. The relationship between the intensity of the diffracted orders and the membrane displacement is given by the following equations [8]:

$$I_0 = I_{in}\left(0.5\cos\left(4\pi\frac{d}{\lambda}\right) + 0.5\right) \tag{4}$$

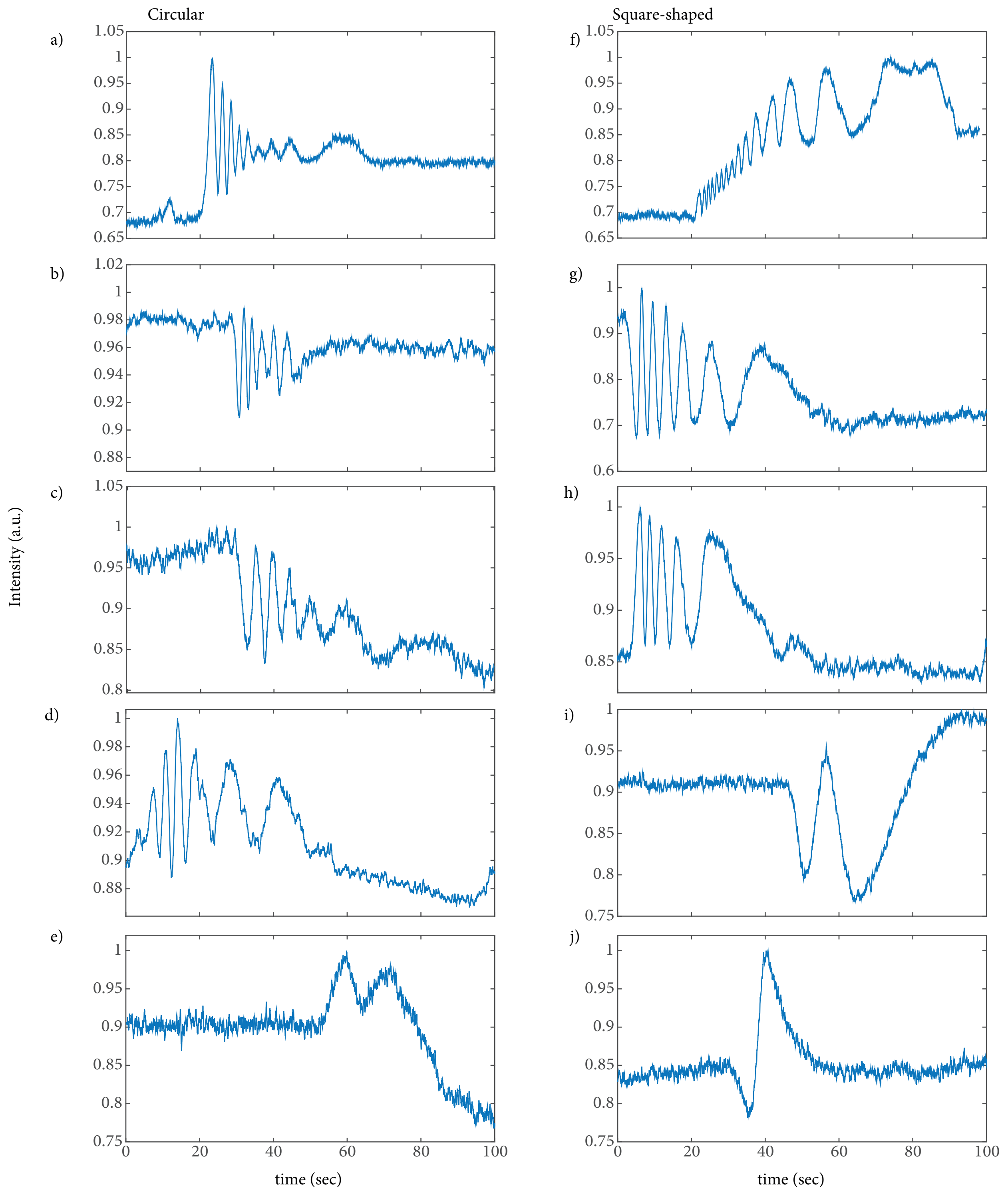

Figure 4. Thermomechanical response of circular MEMS membranes with diameter of a) 1.5 mm, b) 1 mm, c) 750 μm, d) 500 μm, and e) 250 μm, and square-shaped MEMS membranes with width of f) 1.5 mm, g) 1 mm, h) 750 μm, i) 500 μm, and j) 250 μm. A temperature of $\Delta T = 2.5$ $^\circ$C was applied to all sensors except e), i), and j), where $\Delta T = 5$ $^\circ$C was applied to boost the thermomechanical response to reveal adequate number of fringes for precise displacement measurement.

$$I_1 = \frac{4}{\pi^2} I_{in} (0.5 - 0.5cos\left(4\pi \frac{d}{\lambda}\right)) \quad (5)$$

Here, I_{in} is the input laser intensity, d is the sensor gap position, and λ is the laser wavelength. The above interferometric relations, showing the intensity behavior of zero- and first-order diffracted light, reveal a sensor displacement of half a wavelength ($\lambda/2$) per fringe, from which the total displacement and the thermomechanical sensitivity are calculated (through dividing the total displacement by the absolute temperature observed by the digital thermometer). MEMS sensors were tested individually through altering the position of the mother chip with respect to the laser beam via the micromanipulator. The heat source temperature was set to different values (ΔT = 100 °C for devices greater than 0.5 mm size, and ΔT = 200 °C for devices smaller than 0.5 mm size, corresponding to 2.5 °C and 5 °C temperature increase at the location of the MEMS chip, as measured by the digital thermometer) to achieve an appreciable amount of interference fringes, as thermomechanical sensitivity varies from sensor to sensor. Thermomechanical sensitivity was also simulated for all sensors using finite-element analysis (FEA) software (ANSYS) and is tabulated in Table 2 along with the experimental values. Note that the interferometric outputs of the sensors that are shown in Figure 4 do not perfectly follow a sinusoidal trend (rather, they exhibit amplitude modulation and a strong DC bias), as given in Eqs. (4) and (5), due to deviations of the MEMS sensor motion from a perfectly parallel out-of-plane mechanical response. Nevertheless, despite any imperfections in the motion, a fringe in the interferometric output always corresponds to half a wavelength of displacement [9]. Table 1 suggests that the thermomechanical sensitivity scales proportionally with the sensor area. Fitting a quadratic function between the experimentally acquired thermomechanical response (Table 2) and the sensor area reveals a perfect fit for the square-shaped sensors (with an R^2 value of 0.97) and a good fit for the circular-shaped sensors (with an R^2 value of 0.86). Note that the thermomechanical response of the 750 μm circular membrane was omitted from the fit, as it exhibited a deviant response from the rest of the group.

Table 2. Experimental, FEA, and analytical result summary of the tested sensors.

Sensor	Type	Size (μm)	TM response (experiment)	TM response (FEA)	Measurement range <T>	Spring constant (experiment)	Spring constant (FEA)	Time constant (ms)
A	Circular	1500	1143 nm/°C	1633 nm/°C	6.12 °C	4.34 N/m	6.12 N/m	1.31
B	Circular	1000	762 nm/°C	640 nm/°C	15.63 °C	1.94 N/m	3.18 N/m	0.9
C	Circular	750	825 nm/°C	407 nm/°C	24.57 °C	4.69 N/m	5.64 N/m	0.65
D	Circular	500	381 nm/°C	159 nm/°C	62.89 °C	5.94 N/m	12.7 N/m	0.45
E	Circular	250	127 nm/°C	46 nm/°C	217.4 °C	17.82 N/m	50.5 N/m	0.22
F	Square	1500	1905 nm/°C	1790 nm/°C	5.59 °C	3.38 N/m	1.56 N/m	3.27
G	Square	1000	825 nm/°C	921 nm/°C	10.86 °C	4.32 N/m	3.00 N/m	2.18
H	Square	750	762 nm/°C	558 nm/°C	17.92 °C	5.87 N/m	4.98 N/m	1.64
I	Square	500	254 nm/°C	274 nm/°C	36.50 °C	8.84 N/m	10.29 N/m	1.09
J	Square	250	64 nm/°C	79 nm/°C	126.6 °C	29.29 N/m	36.34 N/m	0.55

Furthermore, the spring constants of the MEMS sensors were measured using atomic force microscopy (Bruker Nano) to verify the successful release of the MEMS membrane during the last step of the fabrication process. Table 2 tabulates the measured and simulated (FEA) spring constants of the devices, together with analytically calculated sensor response times and measurement ranges for 10 distinct types of sensors. Findings

reveal a thermomechanical sensitivity range of 64–1905 nm/°C (experimental), stiffness range of 2–29 N/m (experimental), thermal response time range of 0.22–3.27 ms (analytical), and temperature measurement range of 6–217 °C (based on Eq. (2)). The experimental and FEA findings on thermomechanical sensitivity reveal an average percent error of about 50% for all 10 sensors, whereas the experimental and FEA findings on the spring constant give an error of about 40%. The errors are attributed to possible differences between the desired and actual layer thicknesses (likely resulting in some deviation from simulated thermomechanical sensitivity and spring constant values), as well as to the stress that is accumulated on the sensors during the fabrication process. As only a few fringes were observed for the small-sized sensors (<750 μm), an appreciable degree of error is introduced when employing the fringe count method, whereas for large sensors the error is diminished, as a significant number of fringes are observed. Indeed, the difference between experimental and FEA-simulated values for the thermomechanical sensitivity drops to $<35\%$ on average for sensors greater than 0.5 mm in width.

Although no measurement was conducted to reveal residual stress on the sensors, the interference fringe contrast observed for the thermomechanical response graphs (Figure 4) can be used as an indicator of the average tilt angle of the membrane, based on the formulation presented by Ferhanoğlu et al. [9]. Accordingly, the average tilt angles were predicted to be between 4.5 and 6.5 mrad for all the sensors. Although stress levels on certain thin films (nitride, for example) can be reduced through adjusting RF frequency or gas flow rates during a chemical vapor deposition process, mitigating the stress factor on both the parylene and titanium materials is quite cumbersome and is not attempted in this study.

The fiber temperature-sensing architecture, utilizing the thermomechanical MEMS detectors presented in Figure 1b, allows for integration and interchange of the MEMS membranes on a single mode optical fiber to modify the measurement range and response time in accordance with the targeted application. In a real-life fiber optic temperature-sensing scenario, the measurement is carried out from the proximal end in order to move the bulky acquisition components (laser source and detector) away from the fiber distal tip. The second set of experiments involved testing the temperature-sensing of the proposed architecture through recoupling the zero-order diffracted light from the sensor back into the fiber and monitoring its intensity via a photodetector that is placed at the proximal fiber end, as illustrated in Figure 3. For this purpose, the MEMS membrane exhibiting the best signal-to-bias ratio or fringe contrast (1-mm-wide, square-framed sensor) was chosen for the proximal detection experiment. It is worth noting that a high fringe contrast is achieved for sensors exhibiting an out-of-plane displacement without tilting, as well as matching reflectivities for the grating and the reflector that is deposited on the membrane [9]. Figure 5 illustrates the change of zero-order intensity recorded while the temperature of the heat source was altered from 50 °C to 450 °C, corresponding to $\sim$5 °C temperature increase at the sensor location, as observed by the digital thermometer. Total displacement was calculated through stitching the displacements calculated for each individual fringe, based on Eq. (4). Although the unambiguous detection range of the interferometer output is limited by quarter wavelength, multiwavelength detection architectures may be conveniently adapted to the proposed setup to significantly improve the detectable displacement range [10] for direct deduction of the amount of total displacement. The amount of sensor displacement, corresponding to about 17 interference fringes, totals up to 5 μm, revealing a thermomechanical sensitivity of approximately 1000 nm/°C based on the temperature increase recorded by the digital thermometer. The measured thermomechanical sensitivity closely matches the simulated value and the thermomechanical sensitivity value that is calculated based on the distal end measurements (Table 2).

The signal-to-noise ratio (SNR) of 147 is calculated by dividing the total displacement (5 μm) by the displacement noise (34 nm) that is observed during the quiescent period of measurement (between 0 and 40 s

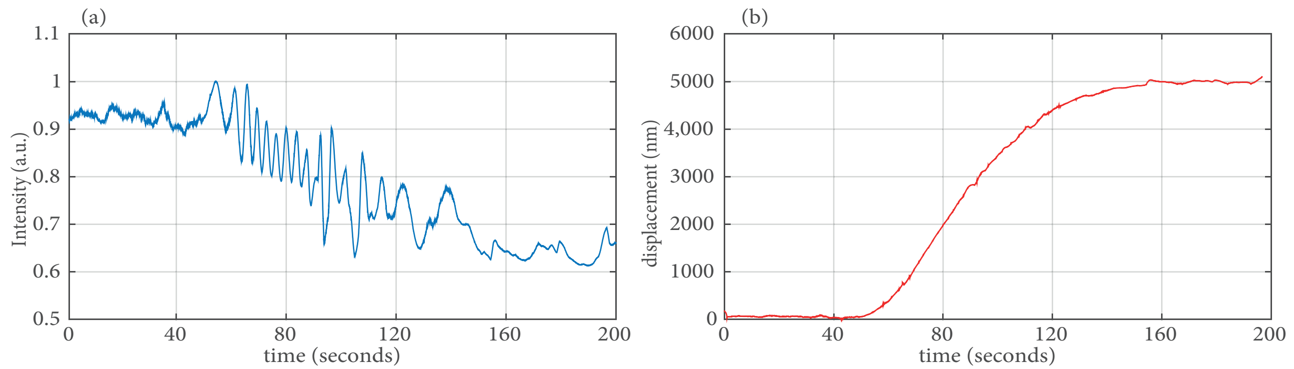

Figure 5. Temperature measurement from the proximal end of the fiber: a) intensity profile, b) calculated displacement.

in Figure 5). Furthermore, temperature sensitivity is calculated as 34 m°C by dividing the total temperature increase (5 °C) by the SNR (147). Note that the fundamental noise component on the zero-order intensity is induced by spurious vibrations, affecting the efficiency of coupling the light back into the fiber. The vibration-associated noise can be lessened through the integration of the MEMS onto the GRIN-collimated fiber, in which case external vibrations will simultaneously affect both the fiber and the MEMS, preserving the coupling efficiency of the laser into the fiber.

4. Conclusion

The design, fabrication, and characterization results of 10 distinct types of MEMS membranes were presented. The MEMS membranes, having embedded diffraction gratings, are suitable for integration into a GRIN-collimated single-mode fiber for temperature measurements via in-line interferometry. The thermomechanical sensitivity of all sensors was thoroughly characterized and simulated, from which the range of temperature measurement was deduced to be between 6 and 217 °C, which is suitable for numerous applications, including the industry and medical fields. The deduced temperature sensitivity of 34 m°C for a selected sensor was achieved despite the use of a low-cost laser and detector, which could be significantly improved upon integration of the MEMS on the fiber, as well as via employing customized laser driving and detector front-end circuitry. The measured temperature sensitivity is comparable to off-the-shelf temperature sensors that can be found on the market, as well as other temperature sensors in the literature [11,12], demonstrating a 10 mK level sensitivity. Finally, the proposed MEMS-on-fiber temperature sensing application allows the replacement of the MEMS sensor for tuning the temperature detection range and speed.

Acknowledgments

This work was supported by the Scientific and Technological Research Council of Turkey (TÜBİTAK, Project No. 114C077). The author acknowledges the support of Hamdi Torun and his research team from Boğaziçi University for fabricating the sensors and assisting with the AFM and SEM measurements; Can Erkey and his research team from Koç University for their support in releasing the MEMS sensors; and Fehmi Çivitci and H Ozan Çirkinoğlu from İstanbul Technical University for useful discussions.

References

[1] Abeysinghe DC, Dasgupta S, Jackson HE, Boyd JT. Novel MEMS pressure and temperature sensors fabricated on optical fibers. J Micromech Microeng 2002; 12: 229-235.

[2] Jo W, Kilic O, Digonnet MJF. Highly sensitive phase-front-modulation fiber acoustic sensor. J Light Technol 2015; 33: 4377-4383.

[3] Çirkinoğlu HO, Bilgin H, Çivitci F, Torun H, Ferhanoğlu O. Fiber temperature sensor utilizing a thermomechanical MEMS detector. J Light Technol 2016; 34: 1025-1030.

[4] Steffanson M, Rangelow I. Microthermomechanical infrared sensors. Optoelectron Rev 2014; 22: 1-15.

[5] Adiyan U, Civitci F, Ferhanoglu O, Torun H, Urey H. A 35-um Pitch IR thermo-mechanical MEMS sensor with AC-coupled optical readout. IEEE J Sel Top Quantum Electron 2015; 21: 87-92.

[6] Torun H, Urey H. Uncooled thermal camera with optical readout. Optoelectron Rev 2006; 14: 54-58.

[7] Datskos PG, Lavrik N V., Rajic S. Performance of uncooled microcantilever thermal detectors. Rev Sci Instrum 2004; 75: 1134-1148.

[8] Hall NA, Lee W, Degertekin FL. Capacitive micromachined ultrasonic transducers with diffraction-based integrated optical displacement detection. IEEE T Ultrason Ferr 2003; 50: 1570-1580.

[9] Ferhanoglu O, Toy MF, Urey H. Fourier optics analysis of grating sensors with tilt errors. Opt Lett 2011; 36: 2254-2256.

[10] Ferhanoglu O, Toy MF, Urey H. Two-wavelength grating interferometry for MEMS sensors. IEEE Photonic Tech L 2007; 19: 1895-1897.

[11] Xu H, Hafezi M, Fan J, Taylor JM, Strouse GF, Ahmed Z. Ultra-sensitive chip-based photonic temperature sensor using ring resonator structures. Opt Express 2014; 22: 3098-3104.

[12] Loranger S, Gagne M, Lambin-lezzi V, Kashyap R. Rayleigh scatter based order of magnitude increase in distributed temperature and strain sensing by simple UV exposure of optical fibre. Sci Rep 2015; 5: 11777-11784.